



GEORG-AUGUST-UNIVERSITÄT
GÖTTINGEN

Fakultät für
Physik 

Bachelor's Thesis

Interpolation von QCD Wirkungsquerschnitten unter Verwendung von APPLGRID und fastNLO

Interpolation of QCD cross sections using
APPLGRID and fastNLO

prepared by

Timo Janßen

from Westerstede

at the II. Physikalisches Institut

Thesis period: April 23, 2015 until July 30, 2015

First referee: Jun.-Prof. Dr. rer. nat. Steffen Schumann

Second referee: Prof. Dr. Arnulf Quadt

Abstract

Timo Janßen

Interpolation of QCD cross sections using APPLGRID and fastNLO

Key words: perturbative QCD; NLO QCD calculations; Monte Carlo event generator; PDF

Contents

1	Introduction	1
2	Theoretical foundations	3
2.1	Basics of perturbative QCD	3
2.1.1	Renormalization and the running coupling	4
2.2	The Parton Model	5
2.2.1	Hadron-Hadron Cross Sections	6
2.3	Corrections to the naive parton model	6
2.3.1	Factorization	8
2.3.2	Evolution	8
2.4	Next-to-leading order calculations	9
2.5	Reweighting QCD calculations	12
2.6	Interpolation grids	14
2.7	The considered process: Higgs production through gluon fusion	16
2.8	Leptonic Higgs decay	19
3	Experimentelle Vorgehensweise	21
3.1	???	21
4	Results	25
4.1	Grid validation	25
4.1.1	Interpolation accuracy	26
5	Diskussion	35

6 Conclusion	37
Appendix	45
Bibliography	45
Todo list	52

CHAPTER 1

Introduction

CHAPTER 2

Theoretical foundations

2.1 Basics of perturbative QCD

QCD is the quantum field theory that describes the strong interactions between Quarks and Gluons. Mathematically, it is a non-abelian gauge theory with symmetry group $SU(3)$. Its Lagrangian is given by

$$\mathcal{L}_{\text{QCD}} = \sum_q \bar{\psi}_{q,a} (i\gamma^\mu \partial_\mu \delta_{ab} - g_s \gamma^\mu t_{ab}^C \mathcal{A}_\mu^C - m_q \delta_{ab}) \psi_{q,b} - \frac{1}{4} F_{\mu\nu}^A F^{A\mu\nu}, \quad (2.1)$$

where the sum goes over all quark flavors. The $\psi_{q,a}$ are quark-field spinors, where $a = 1 \dots 3$ denotes the color index, and the \mathcal{A}_μ^C are gluon fields with a color index $C = 1 \dots 8$. The strong coupling constant is denoted by g_s . Quarks transform under the fundamental representation of $SU(3)$ while gluons transform under the adjoint representation. The t_{ab}^C are the generators of the group. The gluon field tensor $F_{\mu\nu}^A$ is given by

$$F_{\mu\nu}^A = \partial_\mu \mathcal{A}_\nu^A - \partial_\nu \mathcal{A}_\mu^A - g_s f_{ABC} \mathcal{A}_\mu^B \mathcal{A}_\nu^C, \quad (2.2)$$

where the f_{ABC} are the structure constants of the group, defined through $[t^A, t^B] = i f_{ABC} t^C$. In comparison to quantum electrodynamics (QED), the main difference is the presence of the interaction term $-g_s f_{ABC} \mathcal{A}_\mu^B \mathcal{A}_\nu^C$ which results in the existence of 3-gluon and 4-gluon vertices.

The perturbative approach to QCD is to write the observables as a power series in $\alpha_s = g_s^2/(4\pi)$:

$$F = F^{(1)}\alpha_s + F^{(2)}\alpha_s^2 + \dots , \quad (2.3)$$

where $\alpha_s \ll 1$ so that the series can be truncated after a few terms to obtain a useful approximation. A straightforward way to determine the coefficients is the use of Feynman Diagrams.

2.1.1 Renormalization and the running coupling

Calculations in perturbative QCD involve UV-divergent diagrams such as the one illustrated in fig. 2.1, which gives a contribution to the gluon self-energy. Luckily QCD is a renormalizable theory and therefore the divergences can be handled by regularization and renormalization. As a consequence, the quantities appearing in the Lagrangian (the “bare” quantities) are not the same as the quantities we observe physically. The measured values depend on the energy scale, called *renormalization scale* μ_R , at which they are evaluated. This scale is arbitrary and unphysical and if we consider the whole perturbative series, the scale dependence vanishes. The scale dependence can be described by differential equations known as *renormalization group equations*. For example, the equation for the coupling constant takes the form

$$\frac{d\alpha_s(\mu_R^2)}{d\ln \mu_R^2} = \beta(\alpha_s(\mu_R^2)) = -\alpha_s^2(b_0 + b_1\alpha_s + b_2\alpha_s^2 + \dots). \quad (2.4)$$

The minus sign in eq. (2.4) is responsible for the asymptotic freedom of QCD: As the momentum transfer becomes large, the strong coupling becomes weak so that quarks and gluons nearly behave as if they were free particles.

In leading order the analytic solution for eq. (2.4) is known as *running coupling* and

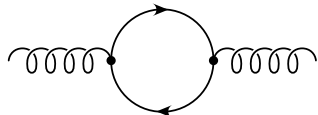


Figure 2.1: UV-divergent loop diagram

given by

$$\alpha_s(\mu_R^2) = \frac{\alpha_s(\mu_0^2)}{1 + b_0 \alpha_s(\mu_0^2) \ln \frac{\mu_R^2}{\mu_0^2}} = \frac{1}{b_0 \ln \frac{\mu_R^2}{\Lambda^2}} \quad \text{with} \quad b_0 = \frac{11N_C - 2n_f}{12\pi}, \quad (2.5)$$

where N_C is the number of colors and n_f denotes the number of flavors. Note that this is only valid at scales where n_f does not change. The first expression uses a reference scale μ_0 , where the value of α_s is known whereas the second one uses the constant Λ , which is the scale where the coupling would diverge.

2.2 The Parton Model

The parton model was introduced in 1969 by Richard P. Feynman to describe high-energy particle collisions involving hadrons [1]. The basic assumption of the parton model is that all hadrons consist of point-like particles (partons) which are responsible for their behavior in interactions. In QCD these can be identified as quarks and gluons. Furthermore, it is assumed that the hadron is in a reference frame where it carries infinite (or at least very high) momentum. In this infinite momentum frame the hadron suffers both Lorentz contraction and time dilation so that the distribution of partons within it does not change during the (vanishingly small) time of interaction. Thus each parton carries a definite fractional momentum x , with $0 < x < 1$. In addition, the process of hadronization due to quark confinement happens too late to influence the interaction. Another important consequence is that the probability of a parton influencing the scattering of another parton is suppressed (“incoherence” of the parton model). The reason this model works is the asymptotic freedom of the underlying theory. However, this also limits the applicability of the parton model to high energy cross sections.

With the help of perturbative QCD, there is a class of reactions involving hadrons for which the cross sections can be calculated directly. These reactions are inclusive and do not contain any hadrons in the initial state. A simple example is lepton pair annihilation into hadrons. As the hadronic final state is fully inclusive, the cross section is identical to the electroweak cross section for $l + l' \rightarrow q\bar{q}$, where l and l' denote leptons and q (\bar{q}) denotes a (anti-)quark. Assuming e^+e^- annihilation and

energies much less than the Z boson mass, the total cross section is therefore given by

$$\sigma_{e^+e^- \rightarrow q\bar{q}}(s) = \frac{4\pi\alpha^2}{3s} \cdot 3 \sum_f Q_f^2, \quad (2.6)$$

where the sum is over all quark flavors that can be produced at the center-of-mass energy \sqrt{s} and the factor 3 is the number of colors [2].

2.2.1 Hadron-Hadron Cross Sections

One of the achievements of the parton model is the prediction of cross sections for hadron-hadron collisions such as the *Drell-Yan process* $h(p) + h'(p') \rightarrow l(k) + l'(k') + X$. That is possible because PDFs are universal between reactions, so they can be determined once and used to calculate different cross sections. In general, the cross section for a hard scattering process involving two initial hadrons can be written as

$$\sigma(p, p') = \sum_{i,j} \int d\xi d\xi' \phi_{i/h}(\xi) \cdot \sigma_{ij}(\xi p, \xi' p', \alpha_s(\mu^2)) \cdot \phi_{j/h'}(\xi'). \quad (2.7)$$

2.3 Corrections to the naive parton model

In order to analyze the effects of higher order corrections, let us reconsider the case of e^+e^- annihilation into hadrons. The Born cross section is given by eq. (2.6). The first correction towards NLO is the emission of a gluon by one of the quarks (see fig. 2.2). Considering soft emission only, one can show that the differential cross

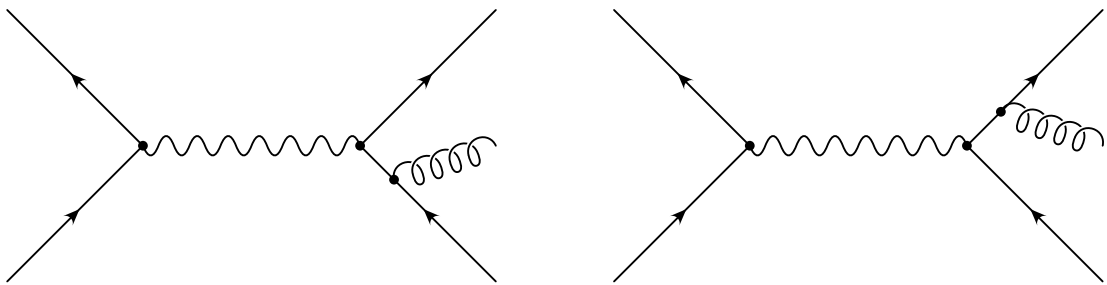


Figure 2.2: Feynman diagrams for gluon emission in e^+e^- annihilation

section for this process factorizes so that one can write

$$|\mathcal{M}_{q\bar{q}g}|^2 d\Phi_{q\bar{q}g} \simeq |\mathcal{M}_{q\bar{q}}|^2 d\Phi_{q\bar{q}} dS . \quad (2.8)$$

The squared matrix element and phase space for $q\bar{q}$ production plus the emission of a soft gluon is given by the Born squared matrix element and phase space multiplied by a factor dS , which is the probability for the emission of a soft gluon:

$$dS = \frac{2\alpha_s C_F}{\pi} \frac{dE}{E} \frac{d\theta}{\sin \theta} \frac{d\phi}{2\pi} . \quad (2.9)$$

There are two divergences in this equation: In the limit $E \rightarrow 0$ there is an infrared divergence and in the limit $\theta \rightarrow 0, \pi$ there is a collinear divergence when the gluon and quark move in the same direction. These divergences always appear when a gluon is emitted by a quark [3].

Additionally to the real emissions in fig. 2.2 there are virtual emissions shown in fig. 2.3, which we have not taken into account yet. As the total cross section must be finite, the divergences in the real term must be canceled by the virtual term (this can, for example, be shown by the use of dimensional regularization [4]). Therefore the corrections to the total cross section are dominated by hard, large-angle gluons and for these perturbation theory is applicable [3]. Observables that are insensitive to the emission of soft or collinear gluons, like the total cross section for $e^+e^- \rightarrow \text{hadrons}$, are called *infrared safe*.

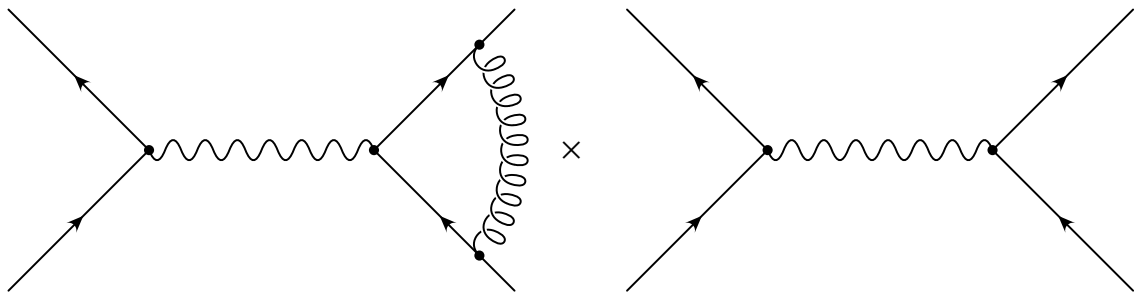


Figure 2.3: Virtual correction in e^+e^- annihilation

2.3.1 Factorization

In processes involving initial-state hadrons, the partons can emit gluons before entering the hard interaction (see fig. 2.4). However, there is an important difference between real and virtual emissions in this case: While the virtual emission does not change the momentum of the parton entering the process, the real gluon carries off parts of the parton momentum. Thus, the total cross section consists of two different hard cross sections that do not cancel in the collinear limit. This is a consequence of the collinear limit corresponding to long-range effects of the strong interaction, which are not calculable in perturbation theory.

In order to be able to calculate cross sections with initial-state hadrons, we can take a similar approach as for the renormalization of the coupling constant and introduce a scale variable which we call the *factorization scale* μ_F . All the non-perturbative parts are cut off at μ_F and absorbed into the PDF. There is an arbitrariness in how much of the correction terms is to be factored out. This is defined by the *factorization scheme*. Common schemes include the DIS scheme, in which all non-leading order contributions are absorbed into the PDFs, and the \overline{MS} scheme, in which only the divergent parts are absorbed. Once the factorization scheme has been chosen, it has to be used consistently in all following cross section calculations.

2.3.2 Evolution

There is an analog for the renormalization group equation for factorization, called the Dokshitzer-Gribov-Lipatov-Altarelli-Parisi (DGLAP) equation. For a quark entering

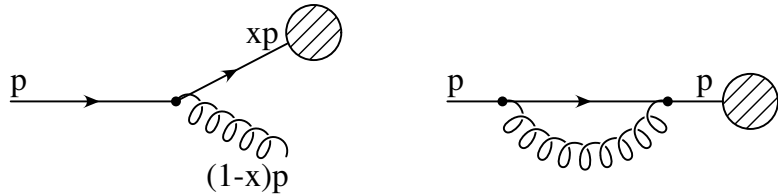


Figure 2.4: Feynman diagrams for initial-state gluon emission

the hard process with longitudinal momentum xp it takes the form

$$\frac{dq(x, \mu_F^2)}{d\ln \mu_F^2} = \frac{\alpha_s}{2\pi} \int_x^1 dz P_{qq}(z) \frac{q(x/z, \mu_F^2)}{z}, \quad (2.10)$$

where $q(x/z, \mu_F^2)$ is the quark distribution. The function $P_{qq}(z)$ is called splitting kernel. It has a perturbative expansion in α_s :

$$P_{qq}(z) = P_{qq}^{(0)}(z) + \frac{\alpha_s}{2\pi} P_{qq}^{(1)}(z) + \dots . \quad (2.11)$$

As the proton does not only contain quarks but also antiquarks and gluons, the actual DGLAP equation is a matrix equation:

$$\frac{d}{d\ln \mu_F^2} \begin{pmatrix} q_i \\ g \end{pmatrix} = \frac{\alpha_s(\mu_F^2)}{2\pi} \begin{pmatrix} P_{q_i q_j} & P_{q_i g} \\ P_{g q_j} & P_{gg} \end{pmatrix} \otimes \begin{pmatrix} q_j \\ g \end{pmatrix}. \quad (2.12)$$

All splitting kernels can be written as perturbative series and have been calculated up to next-to-next-to-leading-order[5, 6]. The DGLAP equation allows to calculate the scale dependence of the PDFs and therefore is an important and powerful tool for PDF fits.

2.4 Next-to-leading order calculations

...(need real and virtual, both separately divergent, need to regularize)

There are two general methods that are commonly used to take care of the infrared divergences in NLO calculations, namely the *slicing method* and the *subtraction method*. We can demonstrate both methods with a simple example similar to the depiction in [7]. Consider the integral

$$I = \lim_{\epsilon \rightarrow 0} \left(\int_0^1 \frac{dx}{x} x^\epsilon F(x) - \frac{1}{\epsilon} F(0) \right), \quad (2.13)$$

where $F(x)$ is an arbitrary function that depends on x . The first term contains a singularity at $x = 0$ and is divergent in the limit $\epsilon \rightarrow 0$. This divergence is canceled by the second term. The parameter ϵ can be compared to the parameter used in

dimensional regularization. As a consequence of $F(x)$ being arbitrary complex, the integral can not be solved analytically. However, in this form it is also not well-suited for a numerical evalution because of the presence of ϵ in the integrand.

In the slicing method, one introduces a small parameter δ , which slices the integration region into two pieces, so that the integral can be written in the following way:

$$\begin{aligned}
I &= \lim_{\epsilon \rightarrow 0} \left(\int_0^\delta \frac{dx}{x} x^\epsilon F(x) + \int_\delta^1 \frac{dx}{x} x^\epsilon F(x) - \frac{1}{\epsilon} F(0) \right) \\
&= \lim_{\epsilon \rightarrow 0} \left(F(0) \int_0^\delta \frac{dx}{x} x^\epsilon - \frac{1}{\epsilon} F(0) \right) + \int_\delta^1 \frac{dx}{x} F(x) + \mathcal{O}(\delta) \\
&= F(0) \lim_{\epsilon \rightarrow 0} \frac{\delta^\epsilon - 1}{\epsilon} + \int_\delta^1 \frac{dx}{x} F(x) + \mathcal{O}(\delta) \\
&= F(0) \ln \delta + \int_\delta^1 \frac{dx}{x} F(x) + \mathcal{O}(\delta).
\end{aligned} \tag{2.14}$$

Therefore, the dependence on ϵ has vanished completely and the remaining integral can be computed numerically. The terms $\mathcal{O}(\delta)$ are neglectable if δ is small. In an actual calculation, one would have to check that the result does not depend on the choice of δ .

The subtraction method does not involve any approximations. Instead, one rewrites the integral in the form

$$\begin{aligned}
I &= \lim_{\epsilon \rightarrow 0} \left(\int_0^1 \frac{dx}{x} x^\epsilon [F(x) - F(0)] + F(0) \int_0^1 \frac{dx}{x} x^\epsilon - \frac{1}{\epsilon} F(0) \right) \\
&= \int_0^1 \frac{dx}{x} [F(x) - F(0)],
\end{aligned} \tag{2.15}$$

which automatically leads to a form that can be evaluated by a numerical integration algorithm. We can take a look at how this method works in a somewhat more realistic calculation. Consider the expression for the expectation value of an infrared-safe observable O at NLO accuracy, consisting of a Born (B), a virtual (V) und a real

(R) term:

$$\langle O \rangle = \lim_{\epsilon \rightarrow 0} \int_0^1 dx x^{-2\epsilon} O(x) \left[\left(\frac{d\sigma}{dx} \right)_B + \left(\frac{d\sigma}{dx} \right)_V + \left(\frac{d\sigma}{dx} \right)_R \right]. \quad (2.16)$$

We assume that the cross sections can be written as

$$\left(\frac{d\sigma}{dx} \right)_B = B\delta(x), \quad (2.17)$$

$$\left(\frac{d\sigma}{dx} \right)_V = a \left(\frac{B}{2\epsilon} + V \right) \delta(x), \quad (2.18)$$

$$\left(\frac{d\sigma}{dx} \right)_R = a \frac{R(x)}{x} \quad (2.19)$$

where B and V are constant factors and $\lim_{x \rightarrow 0} R(x) = B$. a denotes the coupling constant. This model has been adapted from [8]. Obviously, both the real and the virtual part are divergent in the limit $\epsilon \rightarrow 0$. Using the subtraction method analogous to the case above, we can rewrite the real contribution to obtain

$$\begin{aligned} \langle O \rangle_R &= a \lim_{\epsilon \rightarrow 0} \int_0^1 \frac{dx}{x^{1+2\epsilon}} O(x) R(x) \\ &= aBO(0) \lim_{\epsilon \rightarrow 0} \int_0^1 \frac{dx}{x^{1+2\epsilon}} + a \int_0^1 \frac{dx}{x} [O(x)R(x) - BO(0)] \\ &= -aBO(0) \lim_{\epsilon \rightarrow 0} \frac{1}{2\epsilon} + a \int_0^1 \frac{dx}{x} [O(x)R(x) - BO(0)]. \end{aligned} \quad (2.20)$$

By explicitly writing down the virtual part,

$$\langle o \rangle_V = a \lim_{\epsilon \rightarrow 0} \int_0^1 \frac{dx}{x^{2\epsilon}} O(x) \left(\frac{B}{2\epsilon} + V \right) \delta(x), \quad (2.21)$$

we see that the first term gets exactly cancelled by the first term on the right hand side of (2.20). Including the Born contribution we arrive at the expression

$$\langle O \rangle = BO(0) + a \left\{ VO(0) + \int_0^1 \frac{dx}{x} [O(x)R(x) - BO(0)] \right\}, \quad (2.22)$$

which now only consists of finite terms.

The subtraction method can be generalized to arbitrary hadronic cross sections, provided that the definition of the observables allows the cancellation of the divergences. In simplified terms, it always leads to an expression of the form

$$\sigma_{pp \rightarrow X}^{\text{NLO}} = \int d\hat{\sigma}^B + \int d\hat{\sigma}^V + \int d\hat{\sigma}^I + \int d\hat{\sigma}^{RS} \quad (2.23)$$

consisting of a Born (B), a virtual (V), an integrated subtraction (I) and a real subtracted (RS) term. All of these terms are separately finite.

2.5 Reweighting QCD calculations

Often it is needed to vary the parameters in QCD calculations, for example the scale variables and PDFs to estimate the uncertainty. When the number of variations becomes large, it is not practical to rerun the whole event generation for each calculation as the time and resource consumption become too high. Instead it is possible to reuse information from previously generated events and combine them with the new parameters. For a leading order calculation, this is straightforward: Consider the leading order parton model cross section for producing an arbitrary final state X:

$$\sigma_{pp \rightarrow X} = \sum_{i,j} \int dx_1 dx_2 \int d\Phi_n \left(\frac{\alpha_s(\mu_R^2)}{2\pi} \right)^{p_{\text{LO}}} f_i(x_1, \mu_F^2) f_j(x_2, \mu_F^2) d\hat{\sigma}_{ij \rightarrow X}. \quad (2.24)$$

The squared matrix element for the parton-level subprocess $2 \rightarrow n$ is denoted by $d\hat{\sigma}_{ij \rightarrow X}$, differential in the phase space $d\Phi_n$. We can group subprocesses s with the same parton-level cross section into a cumulated parton density $F_s(x_1, x_2, \mu_F^2)$ and write

$$\sigma_{pp \rightarrow X} = \int dx_1 dx_2 \int d\Phi_n \left(\frac{\alpha_s(\mu_R^2)}{2\pi} \right)^{p_{\text{LO}}} F_s(x_1, x_2, \mu_F^2) d\hat{\sigma}_{ij \rightarrow X}. \quad (2.25)$$

Rewriting this in a form that can be computed by a Monte Carlo algorithm on a per-event basis, we arrive at

$$\sigma_{pp \rightarrow X} = \sum_{e=1}^{N_{\text{evt}}} \left(\frac{\alpha_s(\mu_R^2)}{2\pi} \right)^{p_{\text{LO}}} w_e(k_e) F_{s_e}(x_1, x_2, \mu_F^2). \quad (2.26)$$

The event weight $w_e(k_e)$ is given by

$$w_e(k_e) = \Pi_{\text{ps}}(k_e) \Theta(k_e - k_{\text{cuts}}) d\hat{\sigma}_e \quad (2.27)$$

and represents the subprocess cross section $d\hat{\sigma}_e$ with respect to the phase space weight $\Pi_{\text{ps}}(k_e)$ and the kinematic cuts. The kinematic parameters for each event are combined in

$$k_e = \{p_1, \dots, p_n, x_1, x_2\}, \quad (2.28)$$

where the p_i denote the involved partons.

Provided that all event weights have been stored, using a different PDF is as simple as multiplying each weight with the new PDF $F_{s_e}^{\text{new}}(x_1, x_2, \mu_F^2)$. The value of α_s can be changed similarly. To vary the scales, only α_s and F_{s_e} have to be reevaluated as the weights themselves do not depend on the scales.

At NLO the reweighting becomes more involved. The event weights now depend explicitly on the scales and due to the appearance of divergences in the calculation of the parton-level cross sections, a method for cancelling these divergences has to be used. In the following, we will examine the method used by `MCgrid` to reweight NLO calculations. It expects, that the events are generated using the Catani-Seymour dipole subtraction method [9], which is a general algorithm for the automatic calculation of arbitrary jet cross sections at NLO. It is based on the subtraction method introduced in §2.4.

As we have seen, the subtraction method splits the calculation into four parts: The Born (B), virtual (V), integrated subtraction (I) and real subtraction (RS) part. All of these have to be handled differently. How this is done in detail can be seen in the original `MCgrid` paper [10]. The important result is, that if we treat the different

contributions as single events, the NLO result can be written in a form similar to the LO expression (2.26):

$$\sigma_{pp \rightarrow X}^{\text{NLO}} = \sum_{e=1}^{N_{\text{evt}}} \left(\frac{\alpha_s(\mu_R^2)}{2\pi} \right)^{p_e} w_e(k_e) F_{s_e}(x_1, x_2, \mu_F^2), \quad (2.29)$$

where p_e is the order in α_s of the respective event, i.e. $p_e = p_{\text{LO}}$ for B events and $p_e = p_{\text{LO}} + 1$ for I, V and RS events. This allows for simple *a posteriori* parameter variation analogous to the LO case.

2.6 Interpolation grids

Despite the advantage towards regenerating all events for the variation of a single parameter, the reweighting approach is still not a satisfying solution for many use cases. The whole event record has to be stored, which can easily reach many gigabytes in high statistics computations. The storing and reprocessing of the events may be a challenge by itself and is not convenient if more than a few parameter variations have to be performed. One therefore wishes to somehow decrease the resource requirements without losing a significant amount of accuracy. In the ideal case, it should be mostly independent on the statistics. A possible solution is the use of interpolating grids to represent the PDFs and event weights. Then only a uniquely defined number of values has to be saved, while values in-between the grid points are generated by interpolating functions. Such a method has been implemented by the APPLGRID [11] and fastNLO [12, 13] projects.

The PDF $f(x, Q^2)$ depends on the momentum fraction x and the momentum transfer Q^2 . It can be approximated as a sum over discrete grid points using interpolation functions I of order N :

$$f(x, Q^2) = \sum_{i=0}^{N_x} \sum_{j=0}^{N_Q} f(x_i, Q_j^2) I_i^{(N_x)}(x) I_j^{(N_Q)}(Q^2). \quad (2.30)$$

Transferred to the subprocess PDF $F_s(x_1, x_2, Q^2)$ defined above, the interpolation

takes the form

$$F_s(x_1, x_2, Q^2) = \sum_{i,j=0}^{N_x} \sum_{k=0}^{N_Q} F_s(x_i, x_j, Q_k^2) I_i^{(N_x)}(x_1) I_j^{(N_x)}(x_2) I_k^{(N_Q)}(Q^2). \quad (2.31)$$

Consequently, we can write (2.29) as

$$\begin{aligned} \sigma_{pp \rightarrow X}^{\text{NLO}} &= \sum_{e=1}^{N_{\text{evt}}} \sum_{i,j=0}^{N_x} \sum_{k=0}^{N_Q} \left(\frac{\alpha_s(Q_k^2)}{2\pi} \right)^{p_e} w_e(k_e) F_{s_e}(x_i, x_j, Q_k^2) \\ &\quad \cdot I_i^{(N_x)}(x_1) I_j^{(N_x)}(x_2) I_k^{(N_Q)}(Q^2) \\ &= \sum_p \sum_{s=0}^{N_{\text{sub}}} \sum_{i,j=0}^{N_x} \sum_{k=0}^{N_Q} \left(\frac{\alpha_s(Q_k^2)}{2\pi} \right)^p W_{i,j,k}^{(p),(s)}(k_e) F_s(x_i, x_j, Q_k^2), \end{aligned} \quad (2.32)$$

where p is the perturbative order, N_{sub} is the number of different subprocesses and the interpolated weights $W_{i,j,k}^{(p),(s)}(k_e)$ are processed as a sum over the events:

$$W_{i,j,k}^{(p),(s)} = \sum_{e=1}^{N_{\text{evt}}} \delta_{p,p_e} \delta_{s,s_e} I_{i,j,k}^{(N_x)(N_Q)}(k_e) w_e(k_e) I_i^{(N_x)}(x_1) I_j^{(N_x)}(x_2) I_k^{(N_Q)}(Q^2). \quad (2.33)$$

Now the sum over the events is completely absorbed into the definition of the interpolated weights. These can be calculated in a single run of the event generator and be stored efficiently. The calculation of the cross section has become a simple sum over the grid points and thus is much faster for a large number of events. The approach can easily be extended to histogrammed data like differential cross sections by defining the observable bins and computing one weight $W_{i,j,k}^{(p),(s),(b)}$ for each bin b . However, unlike the full event record, the weight grid is restricted to the observable it was constructed for and cannot be used to calculate any other values.

While the variation of the PDF and α_s is still straightforward, scale variation is slightly more complicated because the weights themselves depend on the scale choices. Nevertheless, it is possible to vary the scales without too much effort, using DGLAP evolution. The precise procedure is explained in [11].

2.7 The considered process: Higgs production through gluon fusion

In this thesis, the considered process will be the production of a Higgs boson through gluon fusion. Although there are other possible production mechanisms in the Standard Model, this is the main process at the LHC, with an expected cross section of $\approx 50 \text{ pb}$ at a center-of-mass energy of $\sqrt{s} = 14 \text{ TeV}$ and a Higgs mass of 125 GeV [14]. It proceeds through a triangular loop of heavy quarks (mainly top quarks as the Higgs coupling scales with the quark mass) as is shown in Figure 2.5.

In the narrow-width approximation, the leading order cross section is given by [15]

$$\sigma_{\text{LO}}(pp \rightarrow H) = \sigma_0^H \tau_H \frac{d\mathcal{L}^{gg}}{d\tau_H}, \quad (2.34)$$

where $\tau_H = M_H^2/s$ is the Drell-Yan variable and $d\mathcal{L}^{gg}/d\tau_H$ is the gluon luminosity. The partonic cross section σ_0^H can be written as

$$\sigma_0^H = \frac{G_F \alpha_s^2(\mu_R^2)}{288\sqrt{2}\pi} \left| \sum_q \frac{3}{2\tau_q} \left[1 + \left(1 - \frac{1}{\tau_q} \right) f(\tau_q) \right] \right|^2, \quad (2.35)$$

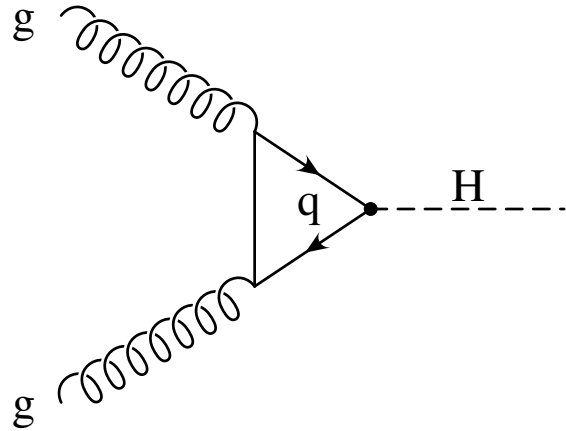


Figure 2.5: Higgs production through gluon fusion.

with the form factor

$$f(\tau_q) = \begin{cases} \arcsin^2(\sqrt{\tau_q}), & \tau_q < 1, \\ -\frac{1}{4} \left[\ln \frac{1+\sqrt{1-\tau_q^{-1}}}{1-\sqrt{1-\tau_q^{-1}}} - i\pi \right]^2, & \tau_q > 1, \end{cases} \quad (2.36)$$

where G_F denotes the Fermi coupling constant and $\tau_q = m_H^2/4m_q^2$. The gluon luminosity takes the form

$$\frac{d\mathcal{L}^{gg}}{d\tau_H} = \int_0^1 dx_1 dx_2 g(x_1, \mu_F^2) g(x_2, \mu_F^2) \delta(x_1 x_2 - \tau_q) \quad (2.37)$$

with $g(x, \mu_F^2)$ denoting the gluon PDF.

The QCD corrections are composed of virtual corrections to the vertices and propagators, real gluon radiation in the initial state and the contributions of the subprocesses $gq \rightarrow Hq$ and $q\bar{q} \rightarrow Hg$. Exemplary diagrams for the corrections are shown in Figure 2.6.

The NLO QCD corrections to the cross section have been calculated in [16]. They increase the cross section by a factor of 1,5 to 1,7. In the limit where the top quark has infinite mass, $m_t \rightarrow \infty$, the form factor takes the value $\frac{4}{3}$. This allows for an analytical expression for the corrections [17], which is very well suited for numerical calculations. It can be considered as an extension of the Standard Model, where the Higgs boson couples directly to gluons (effective Higgs coupling). In many cases, this is a rather good approximation [18].

The NNLO corrections have been calculated in [19, 20].

A fully differential NNLO calculation exists for $H + 0 -$ jet production [21, 22] and substantial progress has been achieved towards an NNLO calculation of the $1 -$ jet cross section [23]. The fully differential NLO cross section is available for $H + 1 -$ jet [24, 25], $H + 2 -$ jets [26, 27] and $H + 3 -$ jets [28].

The effective Lagrangian for Higgs gluon interaction can be written as [20]

$$\mathcal{L}_{\text{eff}}^{ggH} = -\frac{1}{4v} C_1 G_{\mu\nu}^a G^{a\mu\nu} H, \quad (2.38)$$

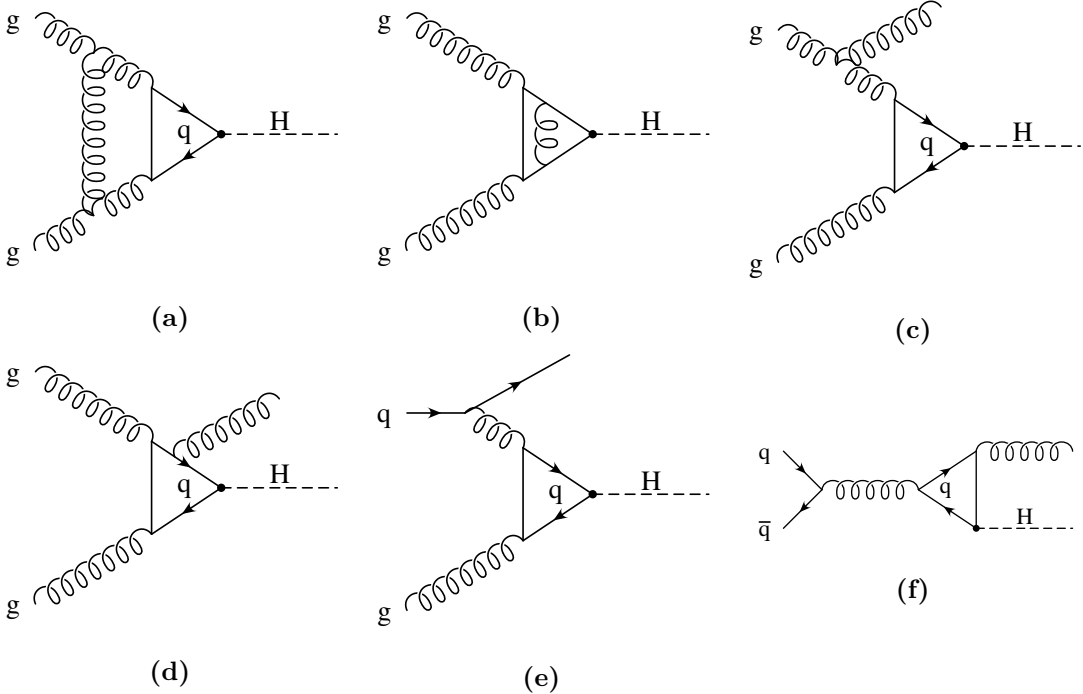


Figure 2.6: Example diagrams illustrating the QCD corrections to the process $pp \rightarrow H$: (a), (b) virtual corrections; (c), (d) real emission of a gluon; (e) $gq \rightarrow Hq$; (f) $q\bar{q} \rightarrow Hg$.

where v is the Higgs vacuum expectation value, $G_{\mu\nu}^a$ is the gluon field strength tensor and H is the Higgs field. The coefficient C_1 , in the $\overline{\text{MS}}$ scheme, is given by

$$C_1 = \frac{-1}{3\pi} \left\{ 1 + \frac{11\alpha_s}{4\pi} + \left(\frac{\alpha_s}{\pi} \right)^2 \left[\frac{2777}{288} + \frac{19}{16} \log \left(\frac{\mu^2}{m_t^2} \right) \right. \right. \\ \left. \left. + n_f \left(-\frac{67}{96} + \frac{1}{3} \log \left(\frac{\mu^2}{m_t^2} \right) \right) \right] + \mathcal{O}(\alpha_s^3) \right\}, \quad (2.39)$$

where the number of active flavors should be set to $n_f = 5$. According to [20], at LO this approximation is accurate within 5 % for $m_H \approx 150 \text{ GeV}$ (which is close to the measured value $m_H \approx 126 \text{ GeV}$) and improves at NLO.

2.8 Leptonic Higgs decay

There are several possible decay channels for the Higgs boson. One has to keep in mind that the Higgs coupling is proportional to the particle masses, so that it will decay into the heaviest possible particles. Assuming a Higgs mass of $m_H = 126 \text{ GeV}$, the most relevant decay products are $q\bar{q}$ (where q denotes a bottom or charm quark), WW , ZZ , $Z\gamma$, $\gamma\gamma$, gg and $\tau^+\tau^-$ [29]. The decay into photons or gluons is only possible through intermediate loops.

The studies leading to the discovery of the Higgs boson at the LHC relied primarily on the decay modes $H \rightarrow \gamma\gamma$, $H \rightarrow ZZ$ and $H \rightarrow WW$.

...For the purpose of this thesis, we will consider the decay $H \rightarrow \tau^+\tau^-$, which has a branching ratio of approximately 6 % [30]. ...There have been searches for $H \rightarrow \tau\tau$ events in the LHC data and both ATLAS [31] and CMS [32] have published evidences for this type of decay.

CHAPTER 3

Experimentelle Vorgehensweise

3.1 ???

APPLGRID and `fastNLO` do not use the momentum fraction x and the factorization scale Q^2 directly in their grids. Instead they provide transformations that are supposed to achieve better coverage of the values. In the following we will concentrate on the x distribution, which is more crucial to the number of grid points needed. The functions provided by APPLGRID are:

$$f_0(x) = \log\left(\frac{1}{x} - 1\right) \quad (3.1)$$

$$f_1(x) = -\log(x) \quad (3.2)$$

$$f_2(x) = \sqrt{-\log(x)} \quad (3.3)$$

$$f_3(x) = -\log(x) + 5 \cdot (1 - x). \quad (3.4)$$

`fastNLO` only provides the functions $f_1(x)$ and $f_2(x)$. To be used in a grid, the functions are divided into equal-sized bins. In order to avoid empty bins, the limit values are determined in a separate “phasespace run” before the actual fill run.

The functions (normalized to the domain $[0, 1]$ for comparability) are shown in Figure 3.1. All transformations increase the point density in the low x region, where most events should fall into. Compared against f_0 , the other functions also accomplish a higher point density in the high x region. Some observables in specific processes might benefit from this.

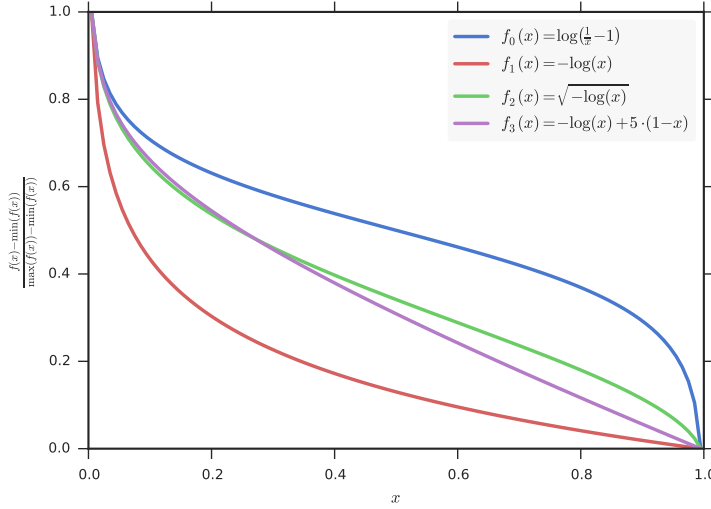


Figure 3.1: The transformations applied to the x distribution, normalized to the range $[0, 1]$.

We can look at the actual x distribution in the process considered in this thesis. In Figure 3.2 it is plotted for one of the gluons involved in the process $gg \rightarrow H + j$ at leading order for a center-of-mass energy of $\sqrt{s} = 13$ TeV. For comparison, the respective distribution for the functions f_1 to f_4 is also shown. In the bare distribution, the number of events per bin increases rapidly towards low x . It is obvious that the reproduction of the low x region is poor for this linear binning. We expect that for some $x > 0$ the number of events approaches zero, because there has to be at least enough momentum transfer to produce the Higgs boson and the jet. To see this with linear binning, one would need a huge amount of bins. In contrast, the transformations are able to project the low x peak to a higher number of bins than the naive linear binning. Additionally, they all approach zero for a finite value (note that high values of $f(x)$ correspond to low values of x). Due to the normalization, this happens at 1. For all transformed distributions, it should be possible to interpolate them with a reasonable number of sampling points. The function $f_1(x)$ looks most promising, as it allocates many bins for the peak region, which should be the most relevant for this process.

If we want to be more specific, we can extract the dependence of the observables

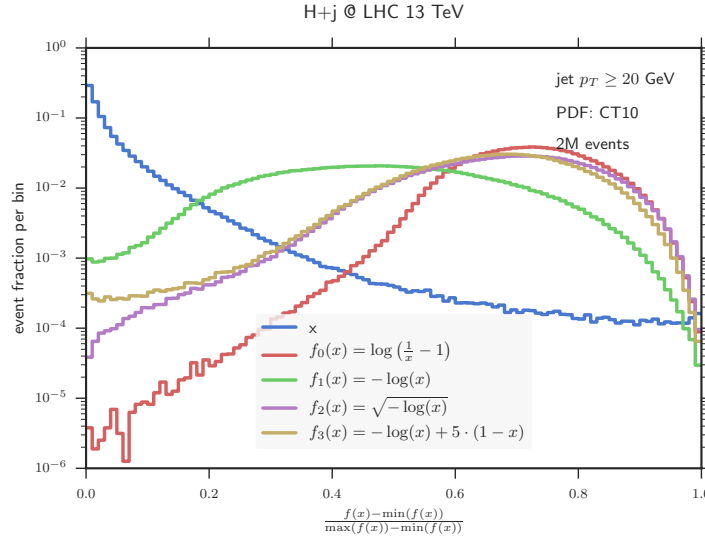


Figure 3.2: The event fraction per bin for the different transformations.

on x and $f(x)$, respectively, from the generated events. This is shown in Figure 3.3 for the transverse momentum p_\perp and in Figure 3.4 for the rapidity y of the Higgs boson. For both observables all considered functions are reasonable. Again, the function $f_1(x)$ seems to be best suited. Hence, it will be the transformation used in all following grid calculations.

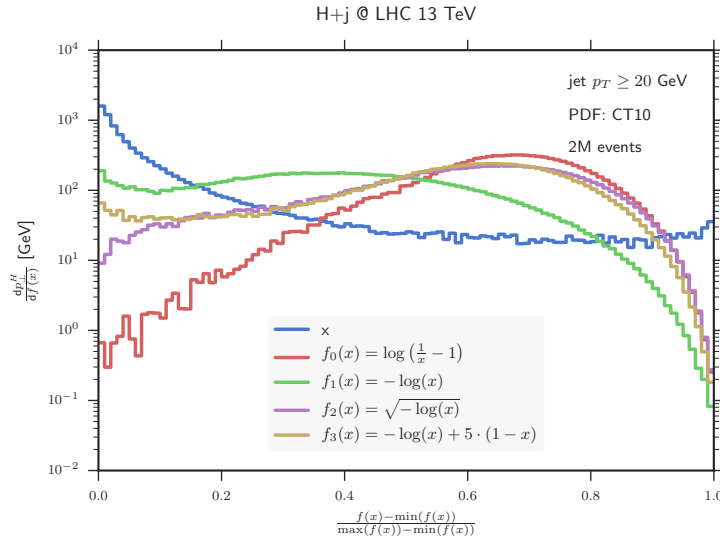


Figure 3.3: The transverse momentum p_\perp of the Higgs boson differential in the momentum fraction x of one of the gluons.

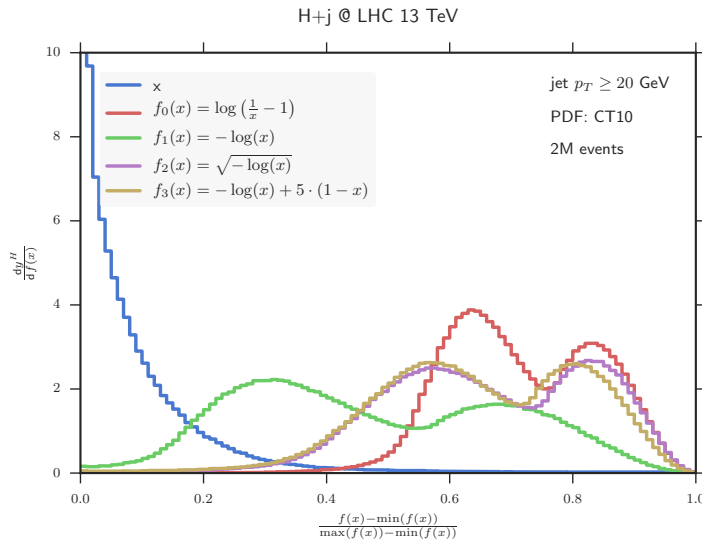


Figure 3.4: The rapidity y of the Higgs boson differential in the momentum fraction x of one of the gluons.

CHAPTER 4

Results

4.1 Grid validation

In the following we will validate the interpolation method used by `MCgrid` for the processes $pp \rightarrow H + (0, 1, 2)\text{jets}$ at the 13 TeV LHC, computed at NLO. Thereto, we generate reference distributions for different observables using the `SHERPA` event generator and compare them to the distributions obtained by convoluting a grid with the respective PDF. When possible, the results from `APPLGRID` and `fastNLO` are compared to each other. All grids are filled using the central value of the CT10 pdf set [33]. The examined observables are the transverse momenta p_\perp of the Higgs boson and the τ leptons, respectively, the rapidity y of the Higgs boson and the pseudorapidity η of the τ leptons. The projection of the observables into histogram bins is accomplished by the `Rivet` analysis system. Final state jets are extracted by the `FastJet` library [34] using the anti- k_t algorithm [35] with a radius parameter $R = 0.4$ and a p_\perp -cut of $p_\perp > 20\text{ GeV}$.

The first validity test will check whether the grids are able to reproduce the distributions when they are filled with the same events as the reference histograms, i.e. when no parameter variation is performed. This will also determine the interpolation accuracy. Subsequently, the cases where the scale factors and/or PDFs of the grids are changed *a posteriori* will be compared to reference distributions where these parameters have been set explicitly.

4.1.1 Interpolation accuracy

In this section we will prove, that the grids are able to reproduce the reference distributions up to the available interpolation accuracy. For each observable, two grids are produced: One high precision grid with 50 bins in x and 30 bins in Q^2 and one lower precision grid with 30 bins in x and $\textcolor{red}{???$ bins in Q^2 . In the 0-jet case, only one Q^2 bin is used, because the scale parameters are fixed to the Higgs boson mass so that Q^2 does not change. To achieve better comparability, APPLGRID is configured to use fourth order interpolation, which is the same as is hardcoded into the **fastNLO** library. A sample of 10 million events is used to fill the grids.

Figure 4.1 shows the ratio of the results obtained by convoluting the grids with the CT10 PDF to the reference distributions. In all cases, the reproduction accuracy is well below 1% and for most of the bins it is even better than 0,1%. The p_\perp distributions produced by APPLGRID are much more sensitive to the grid size than the ones produced by **fastNLO**. For the rapidity distributions, the differnce between the high and the low precision grid is negligible

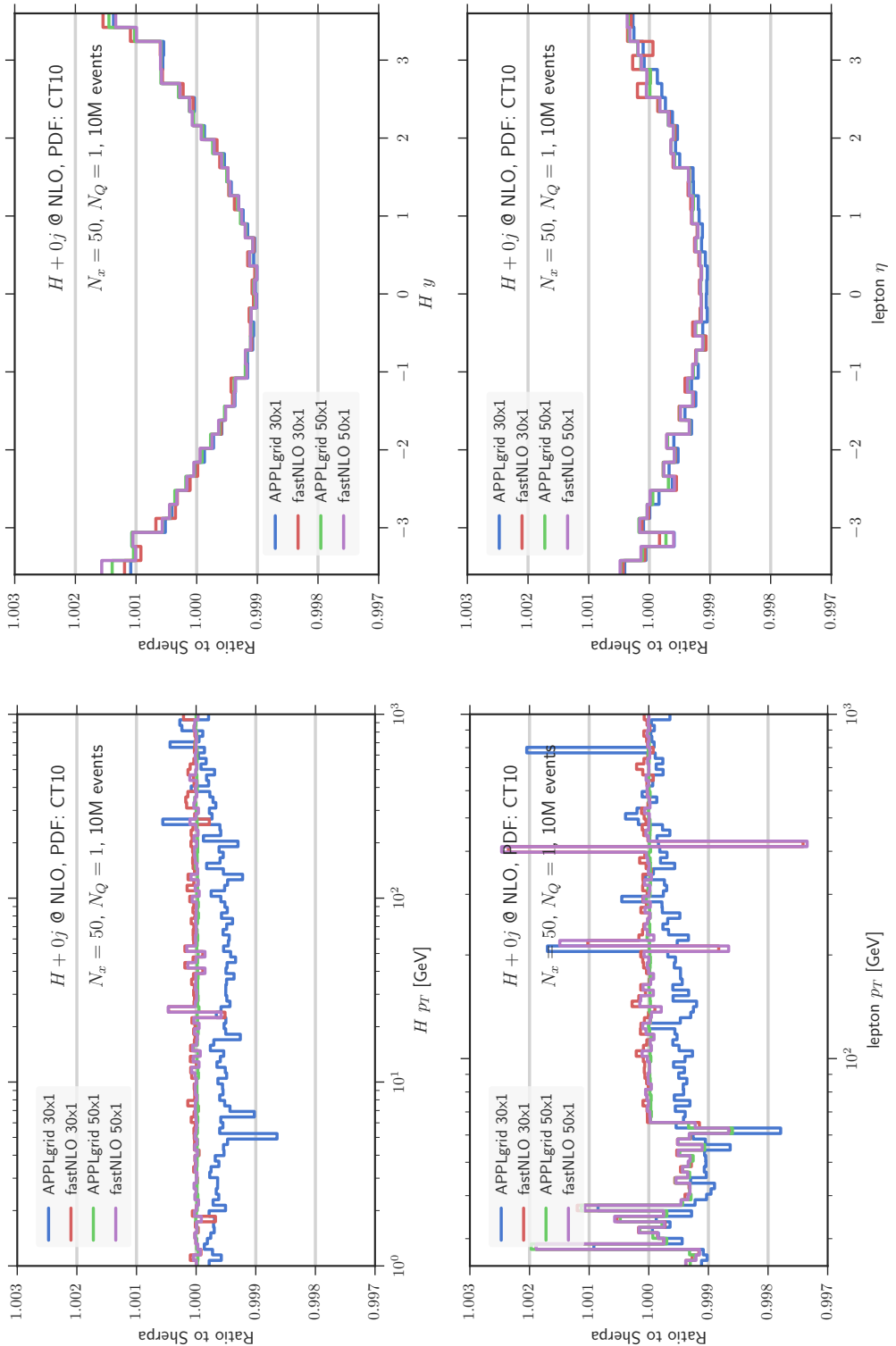
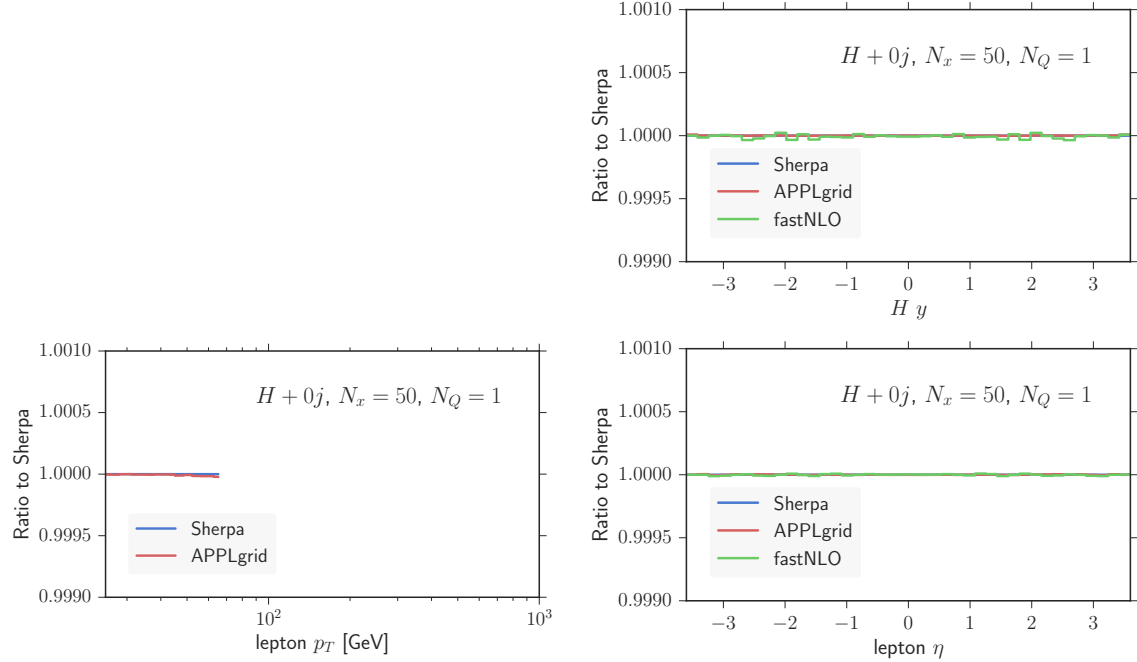
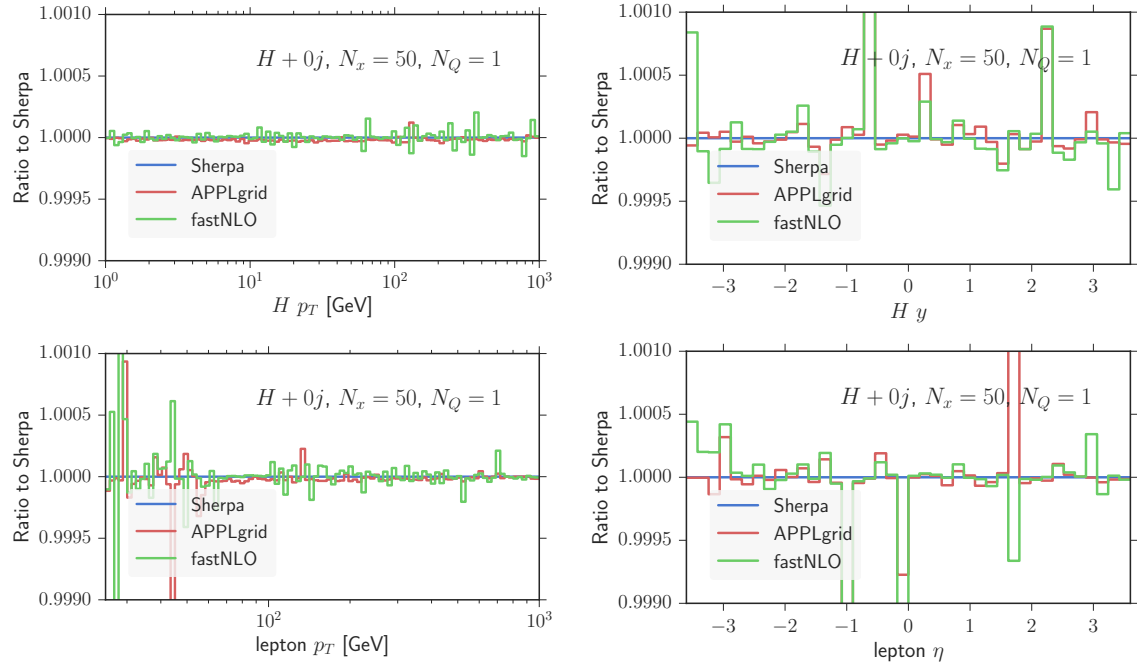
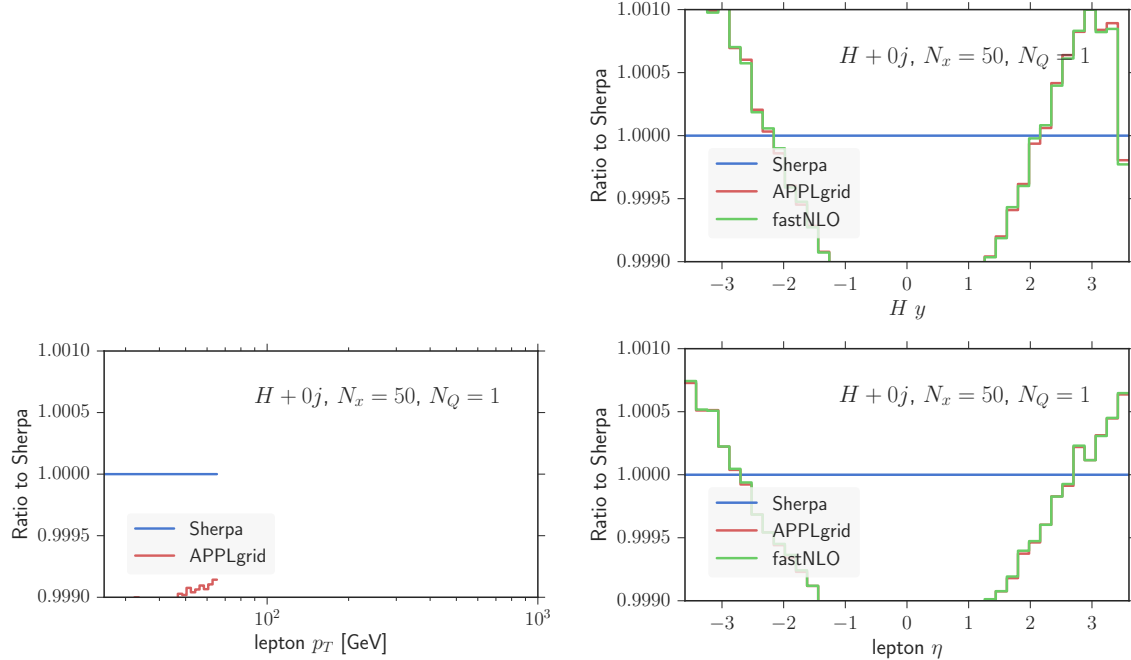
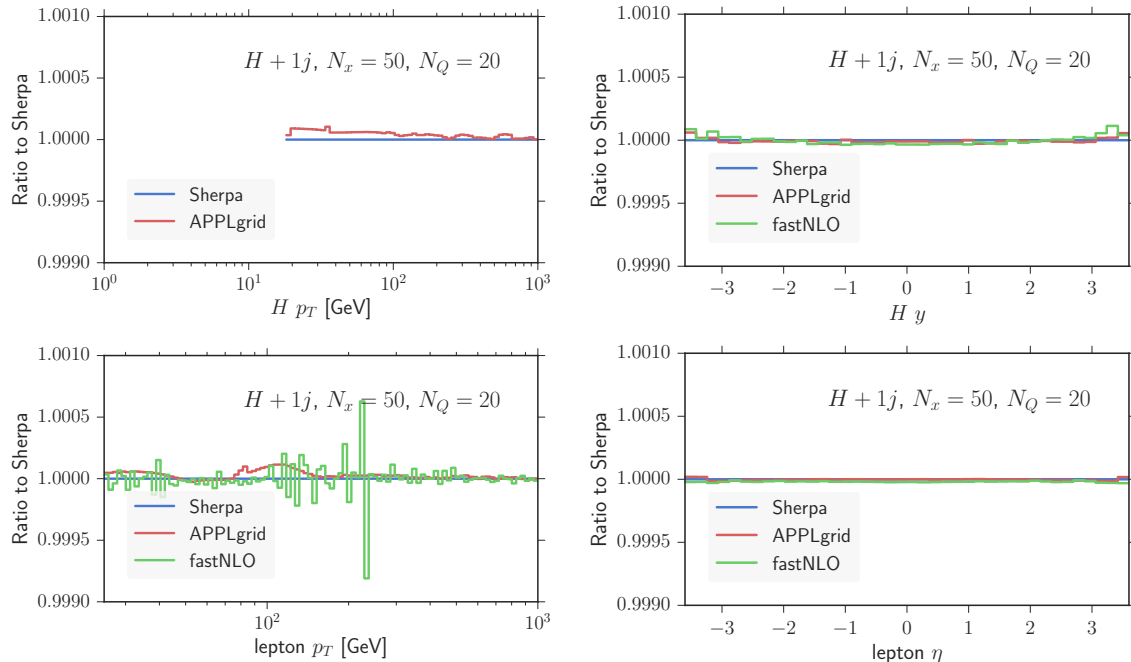


Figure 4.1: $H+0j$ NLO

**Figure 4.2:** H B**Figure 4.3:** H RS

**Figure 4.4:** H VI**Figure 4.5:** Hj B

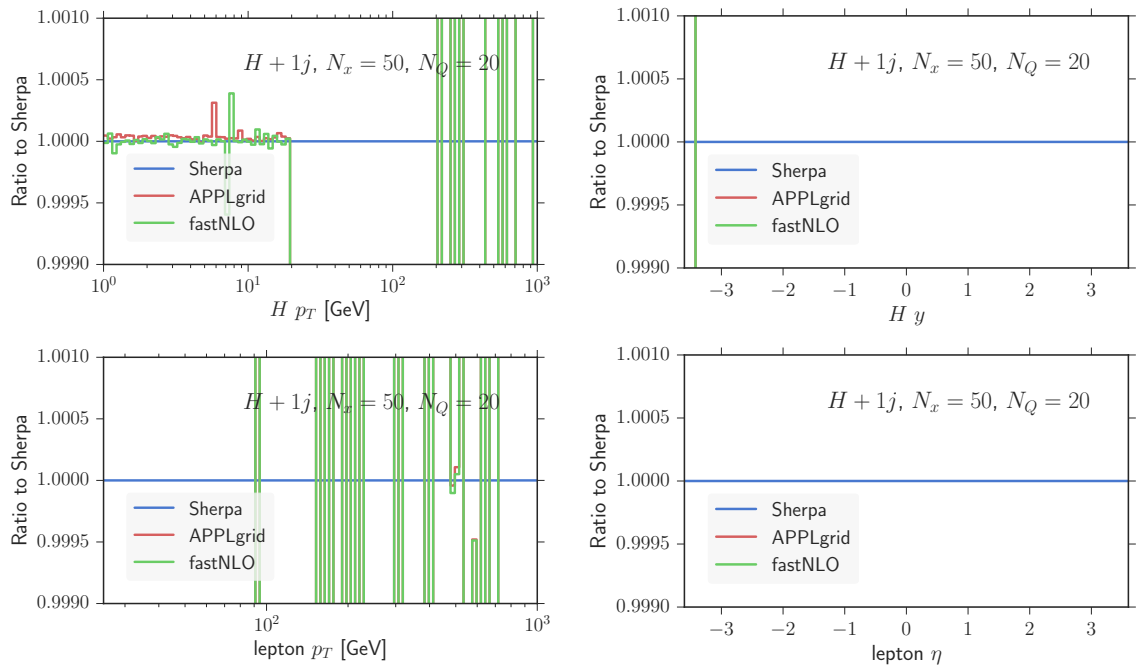


Figure 4.6: $H j$ RS

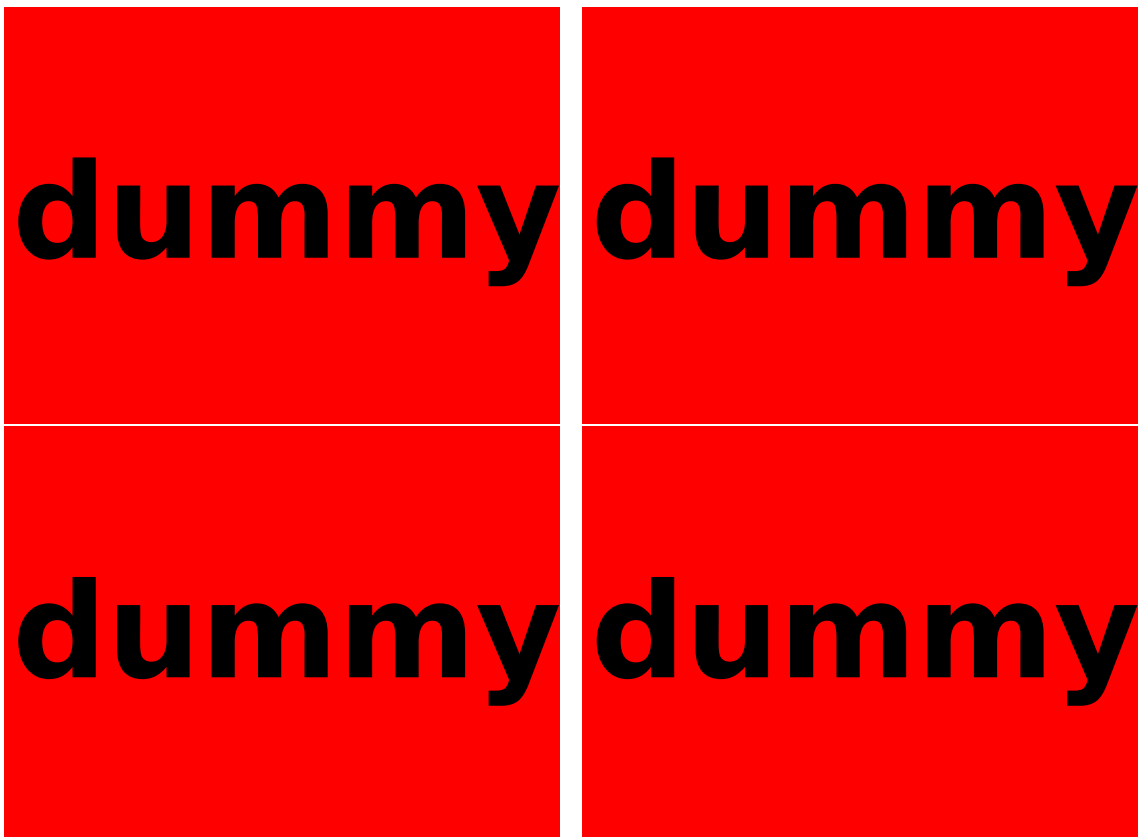


Figure 4.7: Hj VI

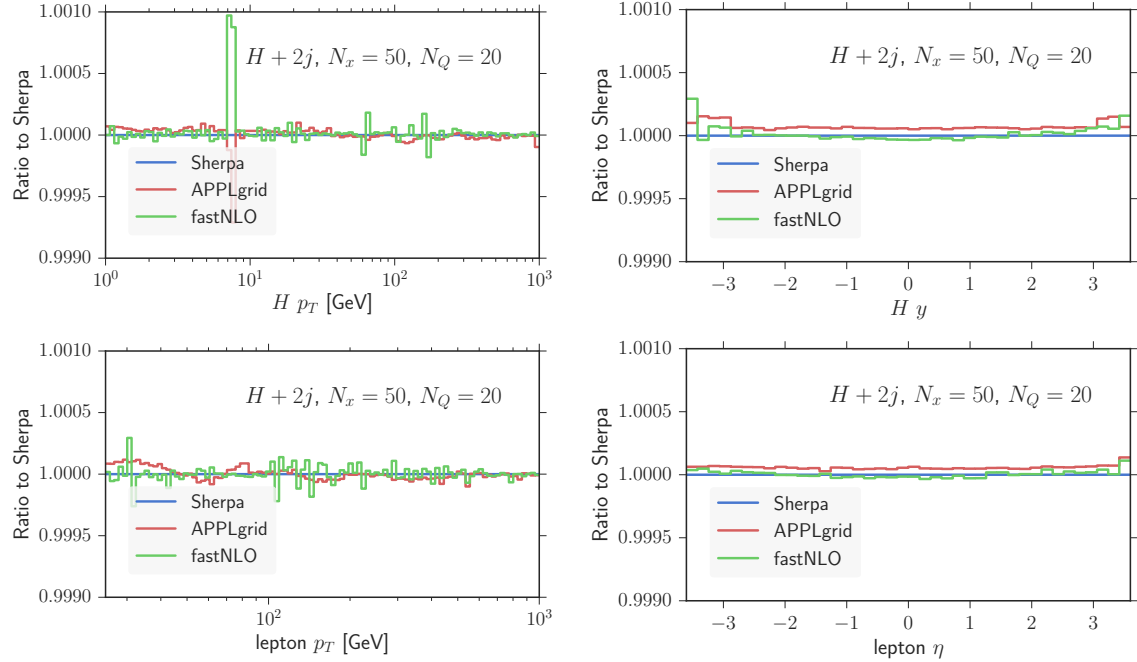


Figure 4.8: Hjj B

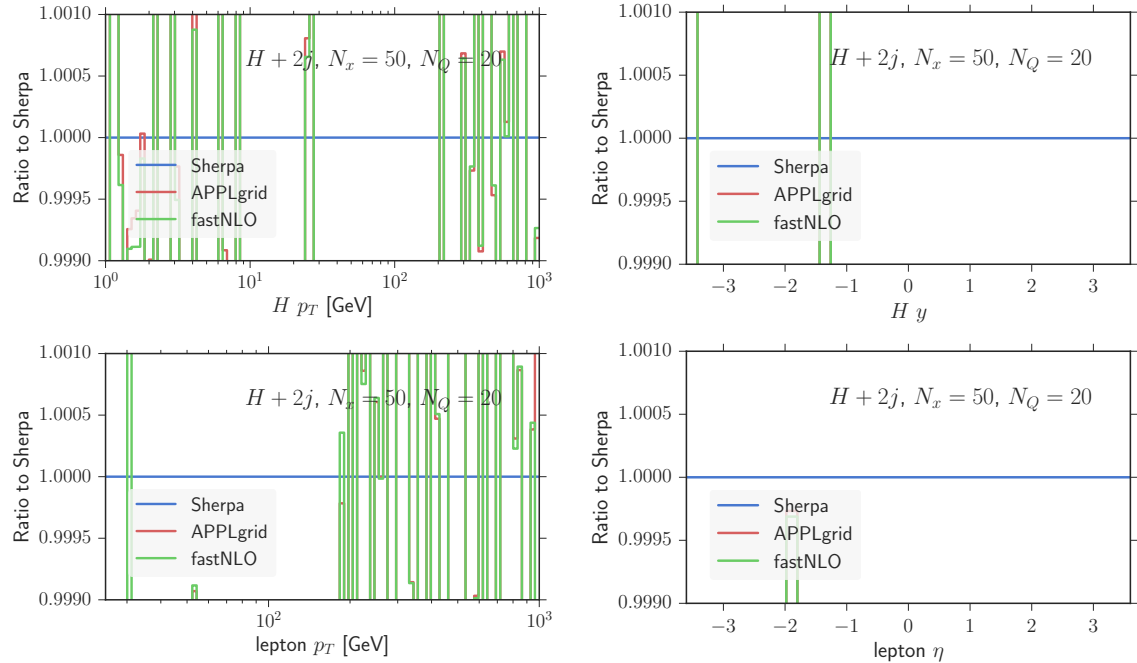
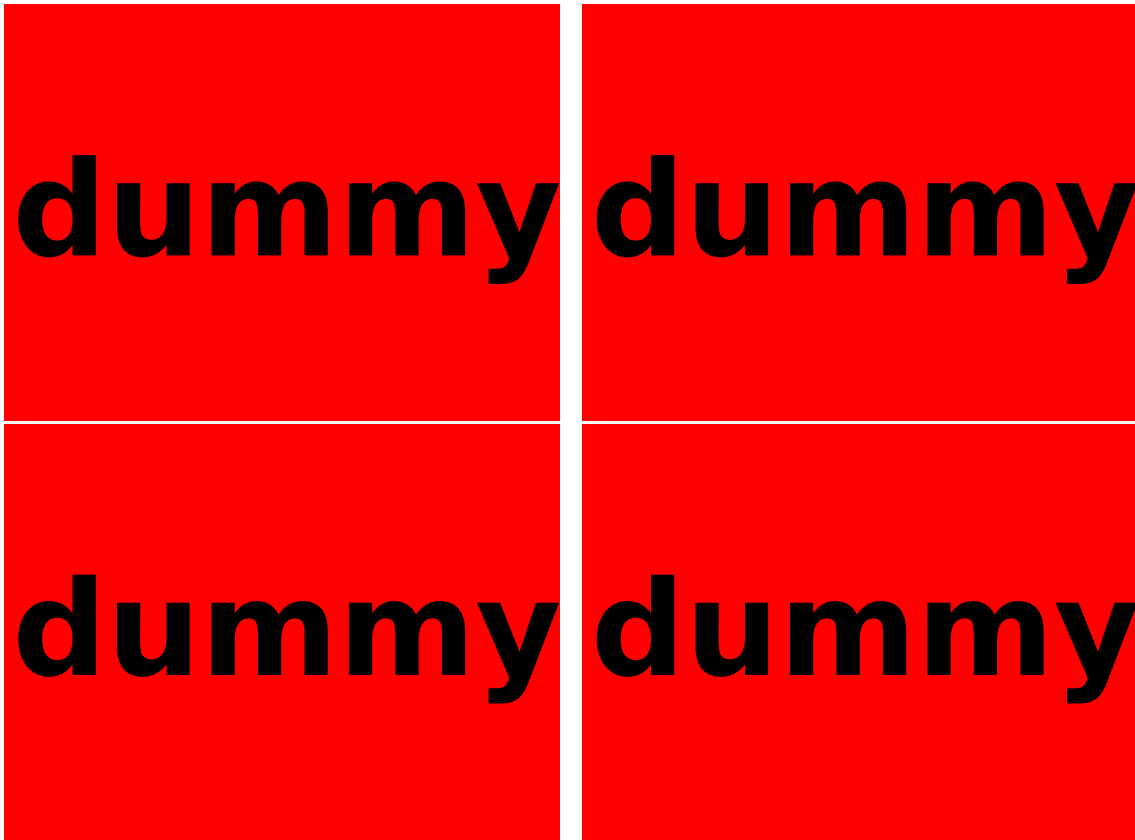
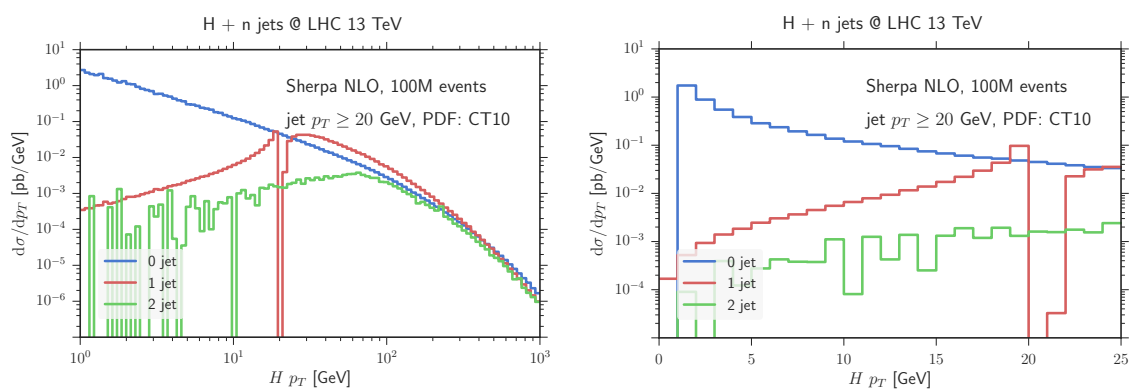


Figure 4.9: Hjj RS

**Figure 4.10:** Hjj VI**Figure 4.11:** H pT NLO (0,1,2) jets

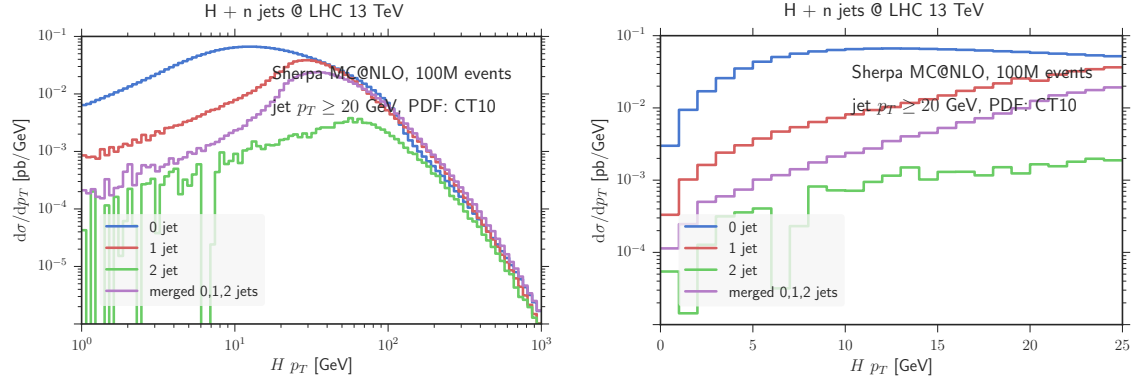


Figure 4.12: H pT MCatNLO (0,1,2) jets

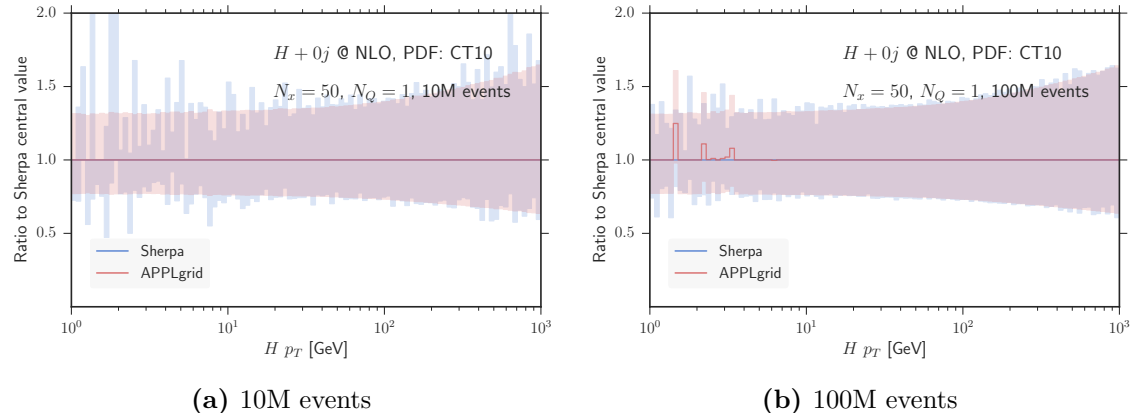


Figure 4.13: Scale variations band

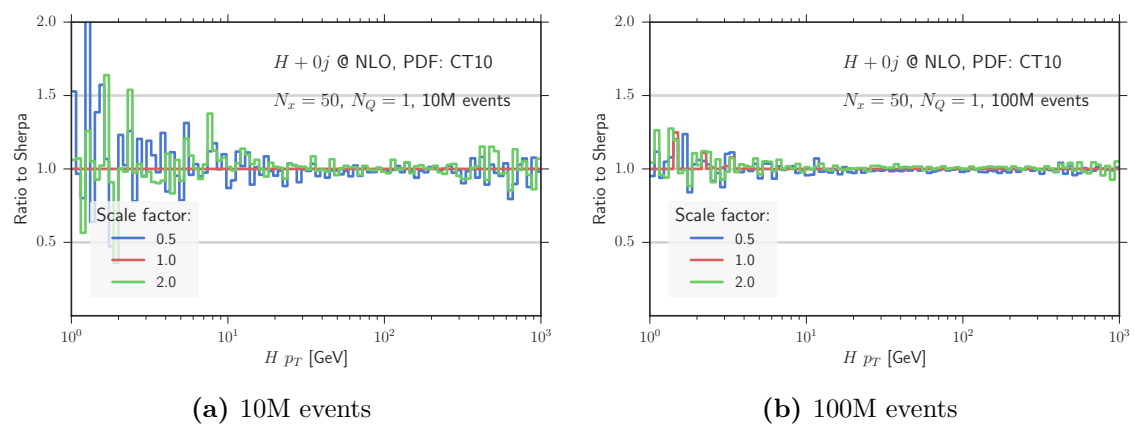


Figure 4.14: Scale variations ratio

CHAPTER 5

Diskussion

CHAPTER 6

Conclusion

...

Version 2.0 of `MCgrid` will allow the creation of grids for calculations matching NLO QCD computations and parton showers using `MC@NLO`. This has not been verified yet for Higgs production. However, as has been seen in section [???](#) the `MC@NLO` approach allows for a more accurate description of soft and collinear emissions than fixed order NLO calculations. Therefore ...

In section [???](#) we examined, how `APPLGRID` and `fastNLO` parametrize the x -distribution to provide a better coverage of the data on a grid with equal-sized bins. Which transformation should be used depends on the considered observable. To achieve the best possible performance, one would have to check the actual x -distribution in each case. The provided transformations are obviously a compromise to cover the needs of a large number of processes. The drawback of this approach is, that for some observables one needs unnecessary large grids to reliably reproduce them. There is, however, an alternative way: When performing the phasespace run prior to the fill run, one could, instead of only determining the limit values of x and Q^2 , sample the whole distribution. By the use of numerical inversion, the data could then be used to provide a transformation that represents the actual distribution of x or Q^2 in the process. Thus, the bins of the grid would be filled ideally and a smaller grid would suffice to reproduce the desired observable. This would improve the overall performance of the software, as a smaller grid means less computation time and less memory consumption.

List of Figures

2.1	UV-divergent loop diagram	4
2.2	Feynman diagrams for gluon emission in e^+e^- annihilation	6
2.3	Virtual correction in e^+e^- annihilation	7
2.4	Feynman diagrams for initial-state gluon emission	8
2.5	Higgs production through gluon fusion.	16
2.6	Example diagrams illustrating the QCD corrections to the process $pp \rightarrow H$: (a), (b) virtual corrections; (c), (d) real emission of a gluon; (e) $gq \rightarrow Hq$; (f) $q\bar{q} \rightarrow Hg$	18
3.1	The transformations applied to the x distribution, normalized to the range $[0, 1]$	22
3.2	The event fraction per bin for the different transformations.	23
3.3	The transverse momentum p_\perp of the Higgs boson differential in the momentum fraction x of one of the gluons.	24
3.4	The rapidity y of the Higgs boson differential in the momentum fraction x of one of the gluons.	24
4.1	$H+0j$ NLO	27
4.2	H B	28
4.3	H RS	28
4.4	H VI	29
4.5	H_j B	29
4.6	H_j RS	30
4.7	H_j VI	31

4.8	Hjj B	32
4.9	Hjj RS	32
4.10	Hjj VI	33
4.11	H pT NLO (0,1,2) jets	33
4.12	H pT MCatNLO (0,1,2) jets	34
4.13	Scale variations band	34
4.14	Scale variations ratio	34

List of Tables

Listings

Bibliography

- [1] R. P. Feynman, Phys. Rev. Lett. **23**, 1415 (1969).
- [2] G. Sterman et al., Rev. Mod. Phys. **67**, www.phys.psu.edu/ cteq/handbook/v1.1/handbook.pdf, 157 (1995).
- [3] G. P. Salam, (2010), arXiv:1011.5131 [hep-ph].
- [4] R. K. Ellis, W. J. Stirling, and B. R. Webber, *QCD and Collider Physics*, Cambridge monographs on particle physics, nuclear physics, and cosmology (Cambridge Univ. Press, Cambridge, 1996).
- [5] S. Moch, J. Vermaseren, and A. Vogt, Nucl.Phys. **B688**, 101 (2004), arXiv:hep-ph/0403192 [hep-ph].
- [6] A. Vogt, S. Moch, and J. Vermaseren, Nucl.Phys. **B691**, 129 (2004), arXiv:hep-ph/0404111 [hep-ph].
- [7] Z. Kunszt and D. E. Soper, Phys. Rev. D **46**, 192 (1992).
- [8] S. Frixione and B. R. Webber, JHEP **0206**, 029 (2002), arXiv:hep-ph/0204244 [hep-ph].
- [9] S. Catani and M. Seymour, Nucl.Phys. **B485**, 291 (1997), arXiv:hep-ph/9605323 [hep-ph].
- [10] L. Del Debbio, N. P. Hartland, and S. Schumann, Comput.Phys.Commun. **185**, 2115 (2014), arXiv:1312.4460 [hep-ph].
- [11] T. Carli, D. Clements, A. Cooper-Sarkar, C. Gwenlan, G. P. Salam, et al., Eur.Phys.J. **C66**, 503 (2010), arXiv:0911.2985 [hep-ph].

- [12] T. Kluge, K. Rabbertz, and M. Wobisch, 483 (2006), arXiv:[hep-ph/0609285](#) [hep-ph].
- [13] M. Wobisch, D. Britzger, T. Kluge, K. Rabbertz, and F. Stober, (2011), arXiv:[1109.1310](#) [hep-ph].
- [14] S. Dittmaier et al., (2011) 10.5170/CERN-2011-002, arXiv:[1101.0593](#) [hep-ph].
- [15] H. M. Georgi, S. L. Glashow, M. E. Machacek, and D. V. Nanopoulos, Phys. Rev. Lett. **40**, 692 (1978).
- [16] D. Graudenz, M. Spira, and P. M. Zerwas, Phys. Rev. Lett. **70**, 1372 (1993).
- [17] A. Djouadi, M. Spira, and P. Zerwas, Physics Letters B **264**, 440 (1991).
- [18] A. Djouadi, Phys.Rept. **457**, 1 (2008), arXiv:[hep-ph/0503172](#) [hep-ph].
- [19] R. V. Harlander and W. B. Kilgore, Phys. Rev. Lett. **88**, 201801 (2002).
- [20] C. Anastasiou and K. Melnikov, Nucl.Phys. **B646**, 220 (2002), arXiv:[hep-ph/0207004](#) [hep-ph].
- [21] C. Anastasiou, K. Melnikov, and F. Petriello, Nucl.Phys. **B724**, 197 (2005), arXiv:[hep-ph/0501130](#) [hep-ph].
- [22] S. Catani and M. Grazzini, Phys.Rev.Lett. **98**, 222002 (2007), arXiv:[hep-ph/0703012](#) [hep-ph].
- [23] X. Chen, T. Gehrmann, E. Glover, and M. Jaquier, Phys.Lett. **B740**, 147 (2015), arXiv:[1408.5325](#) [hep-ph].
- [24] D. de Florian, M. Grazzini, and Z. Kunszt, Phys.Rev.Lett. **82**, 5209 (1999), arXiv:[hep-ph/9902483](#) [hep-ph].
- [25] V. Ravindran, J. Smith, and W. Van Neerven, Nucl.Phys. **B634**, 247 (2002), arXiv:[hep-ph/0201114](#) [hep-ph].
- [26] J. M. Campbell, R. K. Ellis, and C. Williams, Phys.Rev. **D81**, 074023 (2010), arXiv:[1001.4495](#) [hep-ph].
- [27] H. van Deurzen, N. Greiner, G. Luisoni, P. Mastrolia, E. Mirabella, et al., Phys.Lett. **B721**, 74 (2013), arXiv:[1301.0493](#) [hep-ph].

- [28] G. Cullen, H. van Deurzen, N. Greiner, G. Luisoni, P. Mastrolia, et al., Phys.Rev.Lett. **111**, 131801 (2013), arXiv:1307.4737 [hep-ph].
- [29] S. Dittmaier, S. Dittmaier, C. Mariotti, G. Passarino, R. Tanaka, et al., (2012) 10.5170/CERN-2012-002, arXiv:1201.3084 [hep-ph].
- [30] S. Heinemeyer et al., edited by S. Heinemeyer (2013) 10.5170/CERN-2013-004, arXiv:1307.1347 [hep-ph].
- [31] G. Aad et al., JHEP **1504**, 117 (2015), arXiv:1501.04943 [hep-ex].
- [32] S. Chatrchyan et al., JHEP **1405**, 104 (2014), arXiv:1401.5041 [hep-ex].
- [33] H.-L. Lai, M. Guzzi, J. Huston, Z. Li, P. M. Nadolsky, et al., Phys.Rev. **D82**, 074024 (2010), arXiv:1007.2241 [hep-ph].
- [34] M. Cacciari, G. P. Salam, and G. Soyez, Eur.Phys.J. **C72**, 1896 (2012), arXiv:1111.6097 [hep-ph].
- [35] M. Cacciari, G. P. Salam, and G. Soyez, JHEP **0804**, 063 (2008), arXiv:0802.1189 [hep-ph].

Danksagung

Erklärung nach §13(8) der Prüfungsordnung für den Bachelor-Studiengang Physik und den Master-Studiengang Physik an der Universität Göttingen:

Hiermit erkläre ich, dass ich diese Abschlussarbeit selbstständig verfasst habe, keine anderen als die angegebenen Quellen und Hilfsmittel benutzt habe und alle Stellen, die wörtlich oder sinngemäß aus veröffentlichten Schriften entnommen wurden, als solche kenntlich gemacht habe.

Darüberhinaus erkläre ich, dass diese Abschlussarbeit nicht, auch nicht auszugsweise, im Rahmen einer nichtbestandenen Prüfung an dieser oder einer anderen Hochschule eingereicht wurde.

Göttingen, den July 12, 2015

(Timo Janßen)

Todo list
